Journal Name

ARTICLE TYPE

Cite this: DOI: 00.0000/xxxxxxxxxx

Three-Dimensional Atomic Structure of Supported Au Nanoparticles at High Temperature

Pei Liu,[‡a,b] Ece Arslan Irmak,[‡a,b] Annick De Backer,[a,b] Annelies De wael,[a,b] Ivan Lobato,[a,b] Armand Béché,[a,b] Sandra Van Aert,[a,b] and Sara Bals,[*a,b]

Received Date
Accepted Date

DOI: 00.0000/xxxxxxxxxx

Au nanoparticles (NPs) deposited on CeO_2 are extensively used as thermal catalysts since the morphology of the NPs is expected to be stable at elevated temperatures. Although it is well known that the activity of Au NPs depends on their size and surface structure, their three-dimensional (3D) structure at the atomic scale has not been completely characterized as a function of temperature. In this paper, we overcome the limitations of conventional electron tomography by combining atom counting applied to aberration-corrected scanning transmission electron microscopy images and molecular dynamics relaxation. In this manner, we were able to perform an atomic resolution 3D investigation of supported Au NPs. Our results enable us to characterize the 3D equilibrium structure of single NPs as a function of temperature. Moreover, the dynamic 3D structural evolution of the NPs at high temperatures, including surface layer jumping and crystalline transformations, has been studied.

1 Introduction

Understanding the catalytic activity of CeO_2 supported Au nanoparticles (NPs) has been an intensive research topic for the last decades. Indeed, supported Au NPs smaller than 3-5 nm are highly effective catalysts in a wide range of catalytic reactions, e.g. CO oxidation and the water-gas shift reaction[1–5]. It is generally recognized that the activity of Au NPs depends on their size and surface structure. For example, it has been observed that the presence of highly undercoordinated atoms or stepped facets at the surface promotes adsorption of CO molecules or O_2 molecules[1,6,7]. However, the general shape and surface facets of supported NPs are also highly dependent on environmental conditions, such as pressure[8–10] or temperature[11–13]. Quantitative investigations of the atomic configuration at the surface under relevant conditions are thus essential to reveal the active sites of the NPs.

To study these effects, *in situ* transmission electron microscopy (TEM) has been used extensively. For example, it was shown that CeO_2 supported Au NPs yield a rounded morphology in an oxidative atmosphere, whereas they appear faceted in a reducing environment[9]. A reversible dynamics for Au NPs under reactive environments[8–10,14] was furthermore revealed, yielding crystalline transformations[14] but also surface atom diffusion[10]. Phase transformations and morphological evolution of free-standing Au NPs have been extensively studied[11], particularly at temperatures approaching the melting point of Au NPs[9,10]. However, most of these observations are based on two-dimensional (2D) information only, which is not sufficient to connect the entire three-dimensional (3D) structure of the catalysts to their properties.

In the present work, we investigate Au NPs deposited on CeO_2. Supported NPs are used as thermal catalysts since it is expected that the morphology of the NPs is stable at elevated temperatures. Experimentally imaging changes of the 3D atomic structure of catalytic NPs at high temperature, including facet distribution and surface dynamics, is technically challenging but is an essential tool toward design and control over the catalyst structure and performance. Although high-resolution electron tomography has been used to investigate the atomic structure of NPs in 3D, the combination with *in situ* measurements is far from straightforward because of several technical and more fundamental reasons. The main limitation is the time required to collect a tilt series of images, which is typically equal to 1 or several hours[15]. Since catalysts are in active and non-equilibrium states, conventional tomography approaches cannot be applied to investigate the fast changes that supported catalyst NPs undergo when being exposed to a relevant environment. Here, we therefore apply a 3D characterization method that is based on counting the number of atoms in an atomic column from high angle annular dark-field scanning transmission electron microscopy (HAADF-STEM) images and molecular dynamics (MD) simulations to investigate the 3D atomic structure of supported Au NPs[16,17]. This enables us

[a] *Electron Microscopy for Materials Science (EMAT), University of Antwerp, Groenenborgerlaan 171, 2020 Antwerp, Belgium. E-mail: sara.bals@uantwerpen.be*
[b] *NANOlab Center of Excellence, University of Antwerp, Groenenborgerlaan 171, B-2020 Antwerp, Belgium. E-mail: sara.bals@uantwerpen.be*
‡ These authors contributed equally to this work.

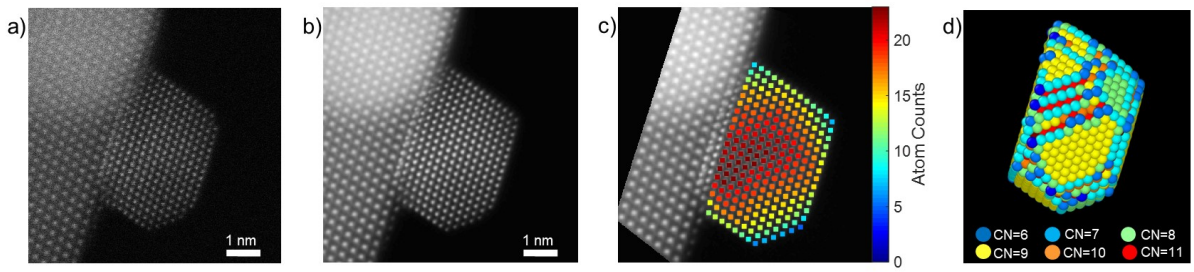

Fig. 1 Schematic illustration of the methodology to obtain a 3D model for Au NPs on a CeO_2 substrate. (a) Raw HAADF-STEM image of a Au NP on CeO_2 support at room temperature. (b) Restored, registered and averaged image (based on ten consecutive frames). (c) Total number of atoms in each atomic column. (d) The final 3D model obtained through MD simulations. The color code corresponds to the coordination number (CN) of each atom. CN=6: atom located on a corner, CN=7: atom located at an edge between two facets, CN=8: atom that is part of a {100} facet, CN=9: atom that is part of a {111} facet, CN=10 or CN=11: atom located in the second layer of an edge, CN=12: inner atom.

to directly estimate the 3D shape of the NP from the experimental observations. In this paper, we first investigate the equilibrium morphology of CeO_2 supported Au NPs at different temperatures in a quantitative manner. Next, we characterize the dynamic 3D structure evolution of the NPs at high temperatures, including surface layer jumping and crystalline transformations.

2 Results and discussion

We have previously shown that the number of atoms in an atomic column of a NP can be counted with single atom sensitivity from HAADF-STEM images, provided that they yield a sufficiently large signal-to-noise ratio (SNR)[17–20]. In order to study the equilibrium shape of the CeO_2 supported Au NPs, ten consecutive time frames were averaged based on a rigid and non-rigid image registration procedure[21]. Prior to averaging, we applied to each individual time frame an in-house developed deep convolutional neural network (CNN) approach for STEM image restoration, enabling us to correct distortions in the images[17]. Figure 1.a shows an uncorrected image of a Au NP on CeO_2 at room temperature. After the averaging of the restored registered time frames (Figure 1.b), we counted the number of atoms in each of the atomic columns of the Au NP with the hybrid statistics-simulations-based atom counting method[19] by taking the detector sensitivity[22] and the temperature-dependent root mean square deviation of Au atoms into account. The counting results, displayed in Figure 1.c, were used to generate a 3D starting configuration by positioning the atoms in each atomic column parallel to the beam direction based on an Au crystalline structure and symmetrically around a central plane. By means of MD simulations that employ the embedded atom method[23], a relaxed 3D model for the structure of the NP was obtained, as illustrated in Figure 1.d. During the MD simulations, the substrate was assumed to have a constant thickness, and a model for CeO_2 was generated based on the fluorite structure[24,25]. To incorporate the interaction between the particle and the substrate, we used the Lennard-Jones potential. All MD simulations were performed by taking the substrate effect into account, although the substrate is not displayed in the figures. More details on the MD simulations are provided in the Methods section. From Figure 1.a, it can be seen that some overlap between Au and CeO_2 appears due to slight tilting of the NP with respect to the electron beam, which creates some artifacts at the interface. Since particle rotation is often observed during the acquisition of a time series of images, the effect of overlap is even more pronounced in the averaged image (Figure 1.b). It should be noted, however, that this interfacial layer was not taken into account during atom counting and did not influence further results.

Using this methodology, we first investigated the thermal stability of a CeO_2 supported Au NP by studying the equilibrium shape and possible facet redistribution as a function of temperature. The averaged HAADF-STEM images of a supported Au NP at different temperatures are displayed in Figure 2.a. The epitaxial relationship between the support and the NP is Au{111}//CeO_2{111}, which is extensively observed for ceria supported Au NPs[9,14]. It can be seen that the 2D projected shape of the NP remains almost the same up to 500 °C. To determine the 3D structure of the particle, we first applied atom counting (Figure 2.b) and found that the total number of detected atoms decreases from 3785 to 3676. Considering the total number of atomic columns indicated in Figure 2.b, this means that on average less than one atom per column disappears, likely because of sputtering caused by the electron beam or due to thermal vibrations, which may complicate the atom detection. Based on the results from atom counting, initial models were created, and MD relaxation was applied for each temperature. Figures 2.c-e show the side, top, and bottom view of the relaxed 3D structures. In accordance with the literature[26,27], the NP has a truncated octahedron shape at room temperature, which is enclosed by {100} and {111} surface facets, as indicated by the color codes explained in Figure 1.d, although small variations can be observed in the coordination number of the atoms located at the {111} interface due to the lattice mismatch between the NP and substrate.

In order to further quantify our results, we determined the coordination number of the atoms at different temperatures (Figure 2.f). As the temperature increases, the percentage of atoms with a coordination number equal to 12 gradually increases, whereas the percentage of atoms with coordination number 10 and 11 decreases since the shape of the NP becomes more symmetric and round. Hereby, atoms will displace from the surface to the interior of the particle. Although there is little change for the coordina-

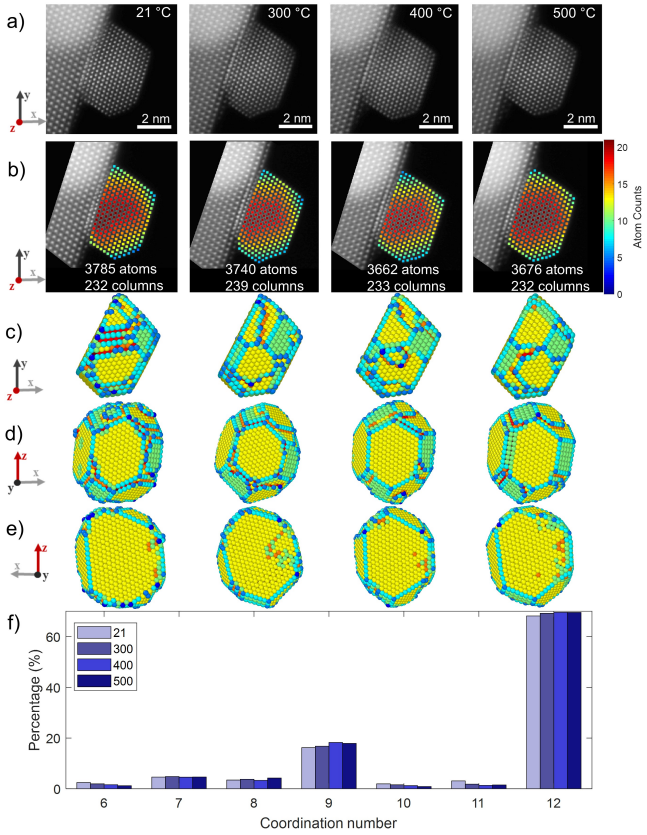

Fig. 2 Structural characterization of a Au NP at different temperatures. (a) Restored, registered and averaged HAADF-STEM images of the Au NP. (b) Atom counting results of the Au NP. The total number of atoms and total number of atomic columns are labeled for each temperature. (c-e) Side, top and bottom view of the relaxed 3D structures. The atoms are presented in different colors according to the coordination numbers (see Figure 1.d). (f) Coordination number histogram of all atoms at different temperatures.

tion numbers as a function of temperature, we do note that the shape of the local surface facets changes, as can be seen by comparing the results for different temperatures in Figure 2.c-e. Since the coordination numbers are important in terms of the activity of the NP during catalysis, our quantitative 3D results prove that this specific particle is indeed expected to be thermally stable up to at least 500 °C.

It is known that the equilibrium shape of supported Au NPs depends on their size. Therefore, a comparison for NPs with different sizes is made in Figure 3, where the particle at the right is the same as the one in Figure 2. HAADF-STEM images of the nanoparticles having a different number of atoms are shown in the first row. In addition to the size effect, the lattice mismatch between the Au NP (4.07 A°) and oxide substrate (5.41 A°) can also affect the shape of the supported NPs[23,24,26]. Therefore, the positions of the atomic columns were fitted using statistical parameter estimation theory, and the projected atomic displacement maps of each NP were extracted according to the ideal positions of the Au atoms. The displacement maps are shown in the second row of Figure 3. Then, the same methodology as explained above was used to extract the shape and the coordination numbers as a function of temperature. The side and the bottom view of the relaxed 3D structures are illustrated in the third and the fourth row, respectively. Finally, the coordination numbers are shown in the fifth row. According to Figure 3.a, high strain can be observed at the interface between the particle and the oxide substrate at room temperature. At 500 °C, on the other hand, the projected displacement map shows that the strain at the interface of this particle is more relaxed. This is likely related to the observation that the interface area is also reduced from approximately 13.7 nm^2 to 11.9 nm^2, which is measured from the 3D models. Accordingly, the NP grows in height and becomes more rounded and the percentage of 12-coordinated atoms increases significantly. Moreover, the contribution of the edge atoms (7-coordinated atoms) increases, accompanied by a decrease in {100} and {111} facets corresponding to 8 and 9-coordinated atoms. A similar mechanism is observed for the larger particle shown in Figure 3.b. To relax the strain at the interface at high temperature, the area of the interface between the NP and the substrate is decreased from 20.6 nm^2 to 19.4 nm^2, which leads to a small rise in the percentage of atoms with a coordination number equal to 12. On the other hand, as the size of the Au NP increases (Figure 3.c), the transformation of the morphology at higher temperature becomes less apparent, in accordance with literature[26]. As discussed above, although the contribution of the energetically more favorable {100} and {111} facets increase slightly, the interfacial area for the largest Au NP (Figure 3.c) remains stable (around 23 nm^2). Also, the morphology is maintained while increasing the temperature.

Next, we investigated non-equilibrium shape transformations for this type of supported Au NPs. For this purpose, we acquired a time series of images at 400 °C after an initial acquisition time of 0.14 seconds (Figure 4.a). These individual images were restored using the CNN, and in contrast to the procedures for Figures 1-3, no averaging of consecutive images was performed. At these temperatures, it has been shown previously that entire surface layers of atoms abruptly displace, a phenomenon which is referred to as "layer jumping"[10]. To reliably count the number of atoms from a time series of images, we used a hidden Markov model which explicitly models the possibility of structural changes over time[28]. The temporal resolution equals 0.629 s, corresponding to a frame size of 1024 by 1024 pixels and dwell time of 0.5 μs. It should be noted that the temporal resolution could be further improved by decreasing the dwell time and frame size. The atom counting results are displayed in Figure 4.b. The total number of atoms was found to be close to 1125 for all frames, except for frame 3, for which the number of atoms was equal to 1103. This observation is related to the layer jump, which can be seen more clearly in Figure 4.c, illustrating the counting difference between the consecutive frames. The blue color code indicates a decreasing number of atoms, and the red color code corresponds to an increase in the number of atoms. Figure 4 demonstrates that a layer on the (010) surface facet disappears on the third frame and reappears in frame 4.

Based on the counting results, input structures for MD simulations were again created, and the results are illustrated in Figure 4.d and Figure 4.e. It is clear that the NP in Figure 4 has a similar morphology as the particle in Figure 2, with {100} and {111}

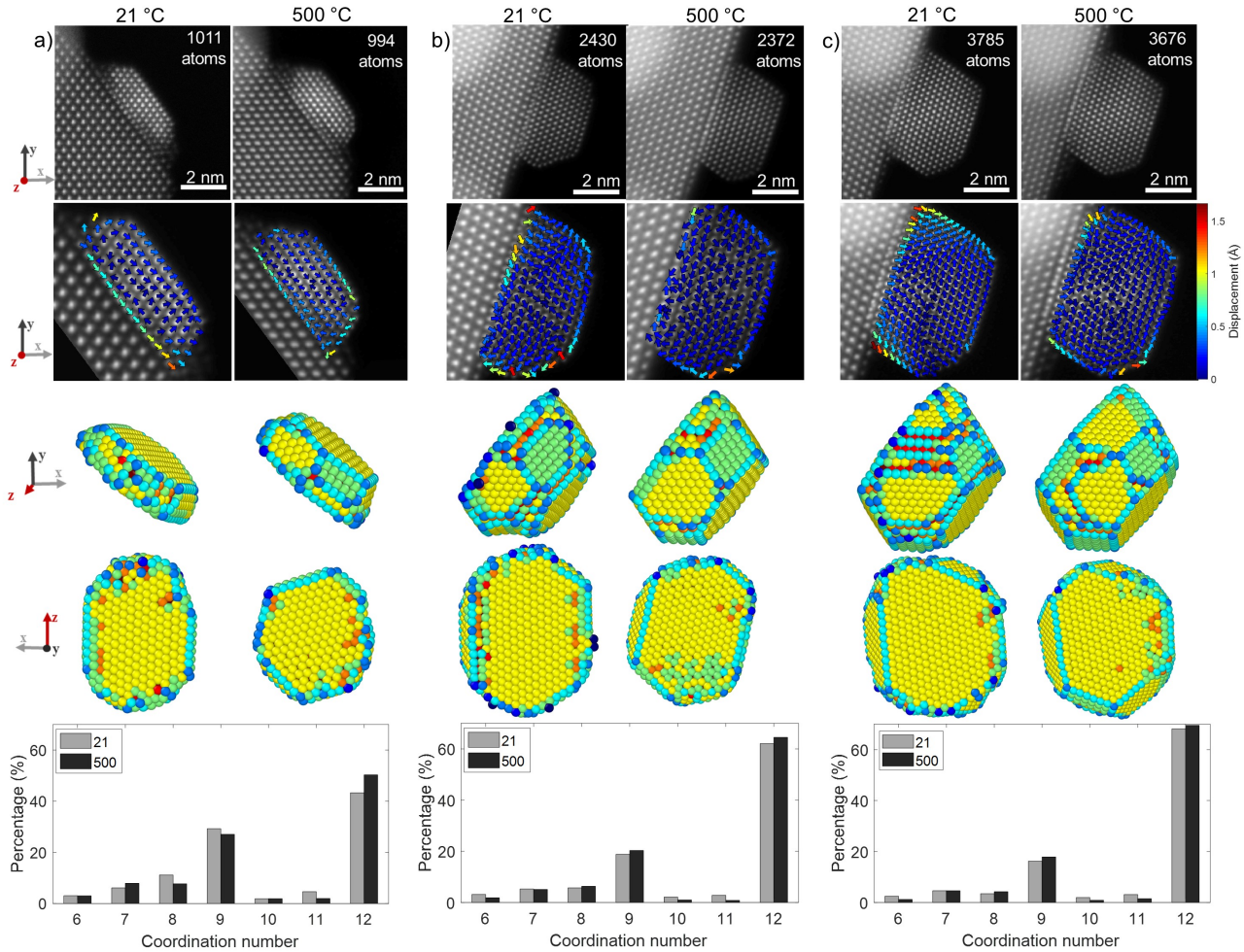

Fig. 3 The 3D structural characterization of the supported Au NPs with different sizes at 21 °C and 500 °C. (a) Au NP having around 1000 atoms. (b) Au NP having around 2400 atoms. (c) Au NP having around 3700 atoms. The atoms are presented in different colors according to the coordination numbers (see Figure 1.d).

surface facets. Based on the 3D models, we can indeed see that an entire (100) plane disappears and reappears (pink atoms in Figure 4.e). Moreover, from the MD simulations, the potential energy was extracted for each system. In the potential energy curve, shown in Figure 4.d, it can be seen that the energy slightly increases after frame 2. This means that the particle becomes less stable around the event of the layer jump. Afterwards, the potential energy decreases and the particle becomes more stable again. It can be seen in Figure 4.e that for the model corresponding to frame 4, the layer (in pink) is not in exact agreement with the original plane (frame 1 and 2) and deviates from a perfect (010) facet. In frame 5, however, the facet is recovered, and the potential energy decreases. Our 3D models indicate that the process of layer jumping cannot be simply considered as a reversible rigid displacement of an entire facet. Indeed, there is a significant change in the surface structure and sites (e.g. frame 3 and 4).

Finally, in addition to changes in the surface structure, we also characterized crystalline transformations that appear for the entire NP at 500 °C. It has been reported that Au NPs in an oxygen atmosphere can transform between two crystalline orientations by electron irradiation or thermal heating since the potential energies of these two orientations are close[14]. These orientations are referred to as Type I: (111)[-110]CeO_2//(111)[-110]Au and Type II: (111)[-110]CeO_2//(111)[1-10]Au. Figure 5 shows an example of a crystalline transformation of a NP which alternates between a Type I and Type II structure, albeit here under high vacuum conditions. The number of atoms for each atomic column is presented in Figure 5.b. Again, no averaging of consecutive frames was performed prior to quantification. Figure 5.c displays the 3D models based on MD simulations, whereas in Figure 5.d, the percentage of internal atoms that can be classified as FCC or HCP is presented, together with the contribution of the disordered atoms. Also the average potential energy per atom for the Au NP was extracted from MD simulations and is displayed in Figure 5.d.

In frame 1 and frame 76, the NP yields a Type II structure, with an FCC internal structure according to the graph in Figure 5.d. In between frame 1 and frame 76, a structural transformation takes place. First, a disordered structure (frame 16) is observed without any ordered facet on the surface (Figure 5.c). Then, a Type I structure is found to be dominant in frame 51, and a twin boundary appears within the NP, which is marked by a dashed white

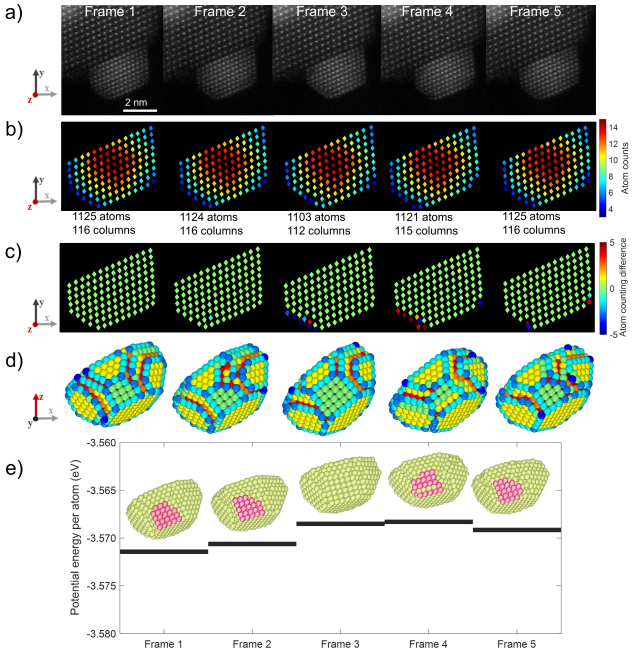

Fig. 4 Reversible shape transformation of the supported Au NP. (a) Time series HAADF-STEM images of a supported Au NP at 400 °C (b) Atom counting results of the Au NP at different time frames. The total number of columns and the total number of atoms are listed for each time snapshot. (c) The change in the number of atoms for all atomic columns between consecutive time frames. (d) 3D relaxed structure of the Au NP at each time frame. The atoms are presented in different colors according to the coordination numbers (see Figure 1.d). (e) Averaged total potential energy per atom for each time shot.

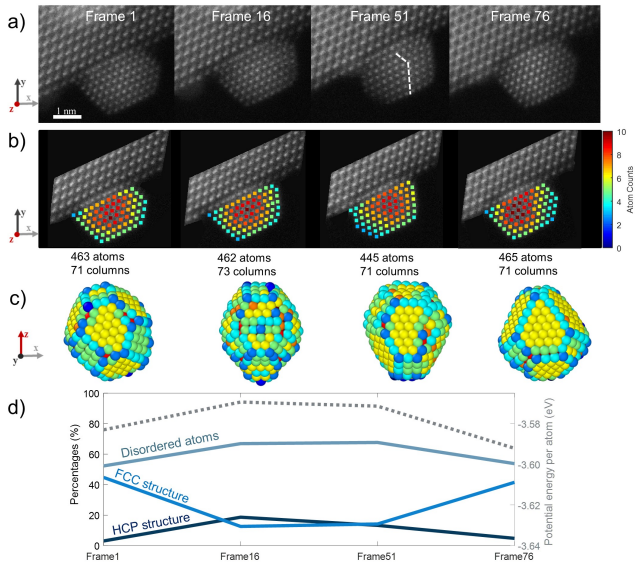

Fig. 5 Crystalline orientation transformation of a supported Au NP. (a) Raw HAADF-STEM images of the supported Au NP at different time frames at 500 °C. (b) Atom counting results of the Au NP at different time frames. The number of columns and the total number of atoms are listed for each time snapshot. (c) 3D models of the supported Au NP. The atoms are presented in different colors according to the coordination numbers (see Figure 1.d). (d) Structural changes and the average potential energy change per atom with the reversible structural transformation.

line in Figure 5.a. As it can be seen in Figure 5.d, this structural transformation is reflected as an increase in the average potential energy per atom and HCP internal structure. In frame 76, the NP has completely transformed back to Type II by having energetically stable {111} and {100} facets, and the potential energy drops again. Moreover, during this reversible transformation, it should be noted that there is always one layer at the interface between the Au NP and oxide support that remains Type II, which indicates the strong interaction between Au and CeO_2.

The surface dynamics of CeO_2 supported Au NPs have been previously investigated by high-resolution TEM. However, given that such images invariably correspond to 2D projections of 3D objects, the interpretation of the particle morphology might be challenging. Conventional electron tomography is not applicable to evaluate the surface structure due to the fast dynamics of the atom movement. The methodology that we present here enables us to go beyond these limitations since we are able to directly describe dynamic changes in the 3D atomic structure in a quantitative manner, also at high temperature. Moreover, it is clear from our experiments that events such as layer jumping or crystalline transformation between type I and II structure are accompanied by intermediate disordered structures with higher potential energies, which may have an influence on the catalytic activity of the particle. Our results can be regarded as realistic 3D input structures and can directly be used as an input for further simulation studies to connect the structure of these catalytic NPs to their activity. The method used in the present work could eventually be extended to a gaseous environment, which will enable real-time 3D characterizations for in-situ and operando catalytic reactions.

3 Conclusions

In conclusion, by combining atom counting based on aberration-corrected HAADF-STEM images and MD relaxation, we were able to perform the atomic-resolution 3D investigation of supported Au NPs. In this manner, we investigated the 3D equilibrium structure of single NPs as a function of temperature. We observed the overall shape appears to become more rounded at higher temperature, especially for relatively small NPs, which might be related to relaxation of interfacial strain. Moreover, we performed an analysis of the surface dynamics, including atomic layer jumping, which is most likely driven by surface atom diffusion. Finally, we characterized the crystalline transformation of a supported NP in 3D at high temperature.

4 Methods

Experimental details. Au/CeO_2 samples were prepared by a physical sputtering coating method. Commercial CeO_2 powder (Sigma-Aldrich) was dispersed in ethanol and drop-casted on a DENSsolutions Nano-chip with a SiNx membrane. The chip was then dried under a lamp for ten minutes and inserted in a sputter chamber. Au NPs were deposited from an Au target using 80 mA current for 5 s in ionized Argon. Next, the chip was mounted in a DENSsolutions Wildfire double tilt holder and inserted into

a Thermo Fisher Scientific Themis Z microscope. After heating at 500 °C in the vacuum of the microscope column for 1h, a model Au/CeO_2 system was obtained for further *in situ* TEM experiments at 300 keV and probe current of 50 pA. The image acquisition parameters of the STEM images, which are shown in each figure, are listed in Table 1.

HAADF-STEM image quantification. A hybrid statistics-simulations-based atom counting method is performed using StatSTEM[19,29]. In this method, the intensities in the HAADF-STEM images are modeled as a superposition of 2D Gaussian functions. Then, the unknown parameters and the volumes under the Gaussian peaks, i.e. the scattering cross-sections, are estimated by fitting an incoherent parametric imaging model to the experimental images using a criterion of the goodness of fit. In a subsequent analysis, the distribution of the scattering cross-sections of all atomic columns is decomposed into overlapping normal distributions. This allows us to count the number of atoms in a particular atomic column with single-atom sensitivity. However, in the absence of a priori knowledge, the results need to be validated with reference scattering cross-section values resulting from accurate multislice simulations. Therefore, frozen phonon calculations by MULTEM[30] are performed to obtain the reference scattering cross-section values by taking the detector characteristics into account due to the non-uniform real detector surface[22]. Moreover, for an accurate quantitative result, the change in root mean square deviation (rmsd) of Au atoms with respect to temperature is considered during the image simulations by using the parameterization for the temperature-dependent Debye-Waller factors[31].

Molecular dynamics simulations. MD simulations are carried out using LAMMPS[32,33]. The simulations are carried out without periodic boundary conditions, and the equations of motion are integrated using the velocity Verlet algorithm with a time step of 0.5 fs. Also, the total linear and angular momenta are conserved so that the supported Au NPs do not drift or rotate throughout our simulation.

First, the energy of the 3D models is minimized using the conjugate gradient method. Then, to obtain the equilibrium shape and structure of the Au NPs at different temperatures, full MD relaxation at experimental temperature is performed in the canonical (NVT) ensemble for 5 ns. However, to investigate the non-equilibrium shapes of the NPs during the reversible structure and shape transformations, the NPs are relaxed for a shorter period of time in order not to result in a more stable but different structure from the experimental observation. Therefore, any deviation from the projected initial atomic column positions is considered as a stopping criterion for the relaxation process. All the 3D structures are visualized by OVITO open visualization tool[34]. Also, the coordination analysis and the polyhedral template matching approach for the structural classification (Figure 5.d) are applied through OVITO Python open-source scripts[35]. For the internal structure characterization of the NPs at 500 °C, the temperature effect is included by considering the parameterized Debye-Waller factors[31] and the temperature-dependent root mean square deviation of Au atoms (rmsd=0.14 at 500 °C).

Author contribution

PL and EAI contributed equally to the paper. The samples were synthesized and HAADF-STEM experiments were performed by PL with the help of AB under the supervision of SB. The images have been corrected for distortions by IL. EAI performed hybrid-statistics-simulations based atom counting and MD simulations with the help of ADB under the supervision of SVA. ADw performed the hidden Markov model for atom counting of time series under the supervision of SVA. The manuscript was written through contributions of all authors. All authors have given approval to the final version of the manuscript.

Conflicts of interest

There are no conflicts to declare.

Acknowledgements

This work was supported by the European Research Council (Grant 815128 REALNANO to SB, Grant 770887 PICOMETRICS to SVA, Grant 823717 ESTEEM3). The authors acknowledge financial support from the Research Foundation Flanders (FWO, Belgium) through grants to A.D.w. and A.D.B. and project funding G.0267.18N.

References

1 B. Hvolbæk, T. V. Janssens, B. S. Clausen, H. Falsig, C. H. Christensen and J. K. Nørskov, *Nano Today*, 2007, **2**, 14 – 18.

2 M. Haruta, N. Yamada, T. Kobayashi and S. Iijima, *Journal of Catalysis*, 1989, **115**, 301 – 309.

3 C. Zhang, A. Michaelides and S. J. Jenkins, *Phys. Chem. Chem. Phys.*, 2011, **13**, 22–33.

4 J. Paier, C. Penschke and J. Sauer, *Chemical Reviews*, 2013, **113**, 3949–3985.

5 Y.-G. Wang, D. Mei, V.-A. Glezakou, J. Li and R. Rousseau, *Nature Communications*, 2015, **6**, 6511.

6 R. Meyer, C. Lemire, S. K. Shaikhutdinov and H.-J. Freund, *Gold Bulletin*, 2004, **37**, 72–124.

7 G. Mills, M. S. Gordon and H. Metiu, *The Journal of Chemical Physics*, 2003, **118**, 4198–4205.

8 H. Yoshida, Y. Kuwauchi, J. Jinschek, K. Sun, S. Tanaka, M. Kohyama, S. Shimada, M. Haruta and S. Takeda, *Science*, 2012, **335**, 317 – 319.

9 T. Uchiyama, H. Yoshida, Y. Kuwauchi, S. Ichikawa, S. Shimada, M. Haruta and S. Takeda, *Angewandte Chemie International Edition*, 2011, **50**, 10157–10160.

10 P. Liu, J. Madsen, J. Schiøtz, J. B. Wagner and T. W. Hansen, *Journal of Physics: Materials*, 2020, **3**, 024009.

11 P. Schlexer, A. B. Andersen, B. Sebok, I. Chorkendorff, J. Schiøtz and T. W. Hansen, *Particle & Particle Systems Characterization*, 2019, **36**, 1800480.

12 D. M. Foster, T. Pavloudis, J. Kioseoglou and R. E. Palmer, *Nature Communications*, 2019, **10**, 2583.

13 A. S. Barnard, N. P. Young, A. I. Kirkland, M. A. van Huis and H. Xu, *ACS Nano*, 2009, **3**, 1431–1436.

Table 1 Image acquisition parameters

Parameters	Figure 1-2	Figure 3.a	Figure 3.b-c	Figure 4	Figure 5
Voltage (kV)	300	300	300	300	300
Semi-convergence angle (mrad)	30.0	30.0	30.0	30.4	21.4
Inner Collection angles (mrad)	46.1	46.1	46.1	46.1	46.0
Outer collection angle (mrad)	198.6	198.6	198.6	198.6	215.0
Frame time (s)	2.52	2.52	2.52	0.629	2
Image size (pixels)	2048x2048	2048x2048	2048x2048	1024x1024	512x512
Beam current (pA)	50	50	50	50	50
Dose per frame (e-Å-2)	20506	41049	20506	4800	58894

14 P. Liu, T. Wu, J. Madsen, J. Schiøtz, J. B. Wagner and T. W. Hansen, *Nanoscale*, 2019, **11**, 11885–11891.

15 H. Vanrompay, E. Bladt, W. Albrecht, A. Béché, M. Zakhozheva, A. Sánchez-Iglesias, L. M. Liz-Marzán and S. Bals, *Nanoscale*, 2018, **10**, 22792–22801.

16 A. De Backer, L. Jones, I. Lobato, T. Altantzis, B. Goris, P. D. Nellist, S. Bals and S. Van Aert, *Nanoscale*, 2017, **9**, 8791–8798.

17 T. Altantzis, I. Lobato, A. De Backer, A. Béché, Y. Zhang, S. Basak, M. Porcu, Q. Xu, A. Sánchez-Iglesias, L. M. Liz-Marzán, G. Van Tendeloo, S. Van Aert and S. Bals, *Nano Letters*, 2019, **19**, 477–481.

18 S. Van Aert, K. J. Batenburg, M. D. Rossell, R. Erni and G. Van Tendeloo, *Nature*, 2011, **470**, 374–377.

19 S. Van Aert, A. De Backer, G. T. Martinez, B. Goris, S. Bals, G. Van Tendeloo and A. Rosenauer, *Phys. Rev. B*, 2013, **87**, 064107.

20 A. De Backer, G. Martinez, A. Rosenauer and S. Van Aert, *Ultramicroscopy*, 2013, **134**, 23 – 33.

21 L. Jones, H. Yang, T. J. Pennycook, M. S. J. Marshall, S. Van Aert, N. D. Browning, M. R. Castell and P. D. Nellist, *Advanced Structural and Chemical Imaging*, 2015, **1**, 8.

22 F. F. Krause, M. Schowalter, T. Grieb, K. Müller-Caspary, T. Mehrtens and A. Rosenauer, *Ultramicroscopy*, 2016, **161**, 146 – 160.

23 G. Grochola, S. P. Russo and I. K. Snook, *The Journal of Chemical Physics*, 2005, **123**, 204719.

24 C. Balaji Gopal, M. García-Melchor, S. C. Lee, Y. Shi, A. Shavorskiy, M. Monti, Z. Guan, R. Sinclair, H. Bluhm, A. Vojvodic and W. C. Chueh, *Nature Communications*, 2017, **8**, 15360.

25 J. L. F. Da Silva, M. V. Ganduglia-Pirovano, J. Sauer, V. Bayer and G. Kresse, *Phys. Rev. B*, 2007, **75**, 045121.

26 C. R. Henry, *Progress in Surface Science*, 2005, **80**, 92 – 116.

27 L. D. Marks and L. Peng, *Journal of Physics: Condensed Matter*, 2016, **28**, 053001.

28 A. De wael, A. De Backer, L. Jones, A. Varambhia, P. D. Nellist and S. Van Aert, *Phys. Rev. Lett.*, 2020, **124**, 106105.

29 A. De Backer, K. van den Bos, W. Van den Broek, J. Sijbers and S. Van Aert, *Ultramicroscopy*, 2016, **171**, 104 – 116.

30 I. Lobato and D. Van Dyck, *Ultramicroscopy*, 2015, **156**, 9 – 17.

31 H. X. Gao and L.-M. Peng, *Acta Crystallographica Section A*, 1999, **55**, 926–932.

32 S. Plimpton, *Journal of Computational Physics*, 1995, **117**, 1 – 19.

33 *LAMMPS Molecular Dynamics Simulator*, `https://lammps.sandia.gov/`.

34 A. Stukowski, *Modelling and Simulation in Materials Science and Engineering*, 2012, **20**, 045021.

35 P. M. Larsen, S. Schmidt and J. Schiøtz, *Modelling and Simulation in Materials Science and Engineering*, 2016, **24**, 055007.